Ceramics International 50 (2024) 37379–37384

Contents lists available at ScienceDirect

Ceramics International

journal homepage: www.elsevier.com/locate/ceramint

Dielectric, electrical and thermal properties of Sodium Molybdate-hexagonal Boron Nitride composites enabled by cold sintering

Javier Mena-Garcia [a,b,*], Michael W. Mervosh [a,b], Pedram Yousefian [a,b], Arnaud Ndayishimiye [b], Steven E. Perini [b], Wenjie Li [a], Bed Poudel [a], Clive A. Randall [a,b]

[a] Department of Materials Science and Engineering, The Pennsylvania State University, University Park, PA, 16802, USA
[b] Materials Research Institute, Millennium Science Complex, University Park, PA, 16802, USA

ARTICLE INFO

Handling Editor by Dr P. Vincenzini

Keywords:
Cold sintering
Dielectrics
Resistivity
Electrical breakdown
Thermal conductivity

ABSTRACT

Advances in 5G and 6G communication technologies and their applications are in part limited by the capabilities of current electronic packaging materials, as expanded bandwidth is a pressing need for novel dielectric substrates capable of co-firing into packages and devices, characterized by low dielectric loss and enhanced thermal conductivity. This investigation provides further characterization in the dielectric, electrical and thermal conductivity properties over previously reported cold sintered composite of Sodium Molybdate $Na_2Mo_2O_7$ (NMO) with hexagonal Boron Nitride (hBN), such as relative permittivity (ε_r) and dielectric loss (tan δ) values at high frequencies of 75–110 GHz, electrical resistivity (ρ) fitting to percolation theory, Weibull statistical analysis of electrical breakdown strength (E_b) and its anisotropic thermal conductivity (κ) influenced by the filler's crystal structure. The cold sintered composites were systematically characterized with respect to filler volume fraction, temperature, and frequency. The findings in this analysis position engineered composites as a promising alternative for microwave substrate materials, with using a densification method that limits interactions and maximizes densification, hence the demonstration with cold sintering.

1. Introduction

Rapid advances in communication technologies and the application of high-power, high-frequency electronics require the development of advanced packaging materials. These materials need to exhibit outstanding properties, such as low sensitivity to temperature changes, reduced dielectric loss (tan δ), and superior thermal conductivity (κ), to support the next generation of technological applications. While increasing the operational frequencies fulfills the need for broader bandwidth for communication technologies, current commercial substrate materials underperform producing significant power dissipation and localized heating extending to nearby components. The development of microwave materials exhibiting excellent thermal conductivity and dielectric performance is the desired solution to provide fruitful alternatives to packaging materials for power electronics. Reported values for common commercial low-temperature cofired ceramics describe dielectric properties of relative permittivity (ε_r) ranging from 4 to 12, dielectric loss ranging from 0.0007 to 0.006 at 1 MHz, and thermal conductivity ranging from 2.0 to 4.5 W m^{-1} K^{-1} [1,2].

Cold sintering is a viable option for the fabrication of such mentioned innovative materials, which viability has been demonstrated for numerous materials systems for a wide extent of applications. A chemo-mechanical process analogous to the pressure solution creep sintering mechanism is characterized by the collective dissolution, mass transport and precipitation in the solid/solvent system. The cold sintering parameters usually occur at temperatures below 300 °C under applied pressures of a few hundred MPa, in the presence of a transient liquid phase which enables the process [3–9]. One of the primary appeals of the cold sintering process lies in its ability to densify bulk and thick film materials for novel composites. The high temperatures used in conventional sintering would introduce chemical reactions and the creation of unwanted secondary phases that would be deleterious to the material's performance and would limit the design of the composite. Cold sintering can circumvent these challenges due to its low temperatures and rapid kinetics, enabling densification of novel material systems. In the design of ceramic matrix composites, the one phase with the major volume fraction (the matrix) would undergo sintering, others (the fillers) can be integrated into the body resulting in a grain boundary engineered

* Corresponding author.
E-mail address: jxm6487@psu.edu (J. Mena-Garcia).

https://doi.org/10.1016/j.ceramint.2024.05.155
Received 29 March 2024; Received in revised form 6 May 2024; Accepted 10 May 2024
Available online 11 May 2024

composite [10–16]. Several studies have demonstrated the successful incorporation of unique composites with polymers (thermoplastics and thermosets) [17] [–] [22], 2-D materials [23,24], and buckminsterfullerene [25], into the grain boundaries of a sintered ceramic material. Previous examples have been made in the cold sintering of low-loss dielectrics with other fillers [26] [–] [37].

Initial results of the microwave properties of Sodium Molybdate-hexagonal Boron Nitride cold sintered composites were published and demonstrated that the composites can be fabricated to maintain high-frequency dielectric properties and high electrical resistivity while simultaneously enhancing thermal properties (thermal conductivity-*k*). This grain boundary engineered composite offers a path for phonon transport in its designed microstructure of interconnected network [38–40]. It has been established that the incorporation of high-κ hexagonal Boron Nitride (hBN) on grain boundaries of Sodium Molybdate (NMO) lead to a higher thermal conductivity, while simultaneously optimizing the dielectric properties for minimal loss. Previous efforts to leverage boron nitride nanosheets, graphene, and diamond nanoparticles have yielded a wide variation in observed effective thermal conductivity [41] and often necessitated a substantial volume fraction of the high-κ filler (50 % or more). Cold sintering can facilitate enhancements by fostering intimate contact between adjacent filler material through confinement of the grain boundary network, as well as a reduction in the required volume fraction of filler needed to reach the percolation threshold where the thermal network can have an observable impact. A very important benefit of the cold sintering process is its capability to produce multilayers with printed electrodes, all of which can be integrated onto metal substrates in a single cold sintering operation. This enhances the viability of cold sintering as a pivotal manufacturing technique for high-frequency and high-power applications in the future [42].

The general goals to be achieved in this investigation are: the fabrication of high density electroceramic composites via cold sintering, using a Sodium Molybdate $Na_2Mo_2O_7$ (NMO) ceramic matrix and hexagonal Boron Nitride (hBN) as a filler with high thermal conductivity; the characterization of physical properties of the composites as a function of filler volume fraction, temperature and frequency; and the fitting and modeling of the measured properties according to their previously reported microstructural design [38].

2. Experimental procedure

Powder synthesis. Stoichiometric amounts of Na_2CO_3 (15.1 g of 99.95 %, Alfa Aesar) and MoO_3 (41.1 g of 99.5 %, Alfa Aesar) were mixed in a PTFE 1 L container, using 8 mm zirconia milling media and 300 ml of ethanol in a ball mill for 24 h. The volume of the container was distributed to be approximately 1/3 zirconia milling media, 1/3 air and 1/3 ethanol plus powder. The resulting slurry was dried for 6 h in a 120 °C oven. This powder was subsequently calcined at 500 °C for 5 h, following the reaction:

$$Na_2CO_3 + 2MoO_3 \rightarrow Na_2Mo_2O_7 + CO_2$$

The $Na_2Mo_2O_7$ (NMO) [43,44] powder was then ball milled under dry conditions for 30 min to break up any formed agglomerates. The final powder displayed an unimodal particle size distribution with a mean size of 2.4 ± 0.9 μm. Further details regarding the NMO powder characterization have been previously reported [38]. The NMO powder was homogeneously mixed with hexagonal Boron Nitride (hBN, 99.8 %, 70–80 nm, Nanoshel) according to the intended filler volume fractions.

Cold sintering process. The proper amounts of NMO and hBN powder were weighed out to fabricate cold sintered composite pellets. These composites contained from 0.5 up to 40.0 vol % hBN. The weighed powders were placed in a glass vial and mixed under dry conditions using a planetary centrifugal mixer (Thinky, AR-250) for 10 cycles of 1 min each. Afterwards, 25 wt % of deionized water was added to the powder as the transient liquid phase, and the materials were mixed in an agate mortar with a pestle until a homogeneous mixture was obtained. The moistened powder was placed in a stainless-steel die for cold sintering. Pellets fabricated for characterization of their dielectric properties were fabricated using a die to make samples of 25 mm diameter and 4 mm thickness, while pellets intended for electrical resistivity, electrical breakdown strength and anisotropic thermal conductivity analysis were fabricated in a die for samples of 13 mm diameter, with thicknesses of 2 mm, 1 mm and 13 mm, respectively. The powder was placed under a uniaxial pressure of 250 MPa (Carver, model CH4386) at room temperature, and then heated at a heating rate of ~15 °C/min up to 180 °C for 2 h using a heating jacket controlled by a Proportional–Integral–Derivative loop feedback mechanism. A thermocouple was placed in a slit at the bottom of the die base. After the 2 h had elapsed, the pellet was ejected from the die and allowed to cool to room temperature. Finally, the pellets were placed in a 200 °C drying oven for 12 h [38]. This curated overall cold sintering procedure yielded relative densities >96 % for NMO pellets and NMO-hBN composite samples with volume fractions of 0–40 vol%. Details about the relative densities and densification process of cold sintered NMO-hBN composites has been previously reported by Mena-Garcia et al. [38] Finally, the surfaces and edges of all samples were manually polished using a 1200 grit silicon carbide sandpaper using ethanol as lubricant. The thickness of pellets fabricated for electrical breakdown testing was reduced by manual polishing from 1 mm to ~0.4 mm.

Characterization. The crystal structure of the synthesized powder was characterized by X-ray diffraction (XRD) analysis using a PANalytical Empyrean system operated at 45 kV and 40 mA with Cu Kα radiation. The NMO particle size distribution was obtained by processing 10,000 X Scanning Electron Microscopy (SEM) images acquired using a Field Emission Thermo Fisher FESEM Verios G4 microscope. Relative densities were calculated by dividing the measured geometrical density of the pellets by their theoretical density ($\rho_{NMO} = 3.682$ g/cm^3, $\rho_{hBN} = 2.1$ g/cm^3). Details on the characterization of SEM and XRD analysis, are previously reported by Mena-Garcia et al. [38].

To assess dielectric properties, 25 mm diameter and 4 mm thick pellets were prepared, and their top, bottom and edge surfaces manually polished with 1200/P4000 Silicon Carbide sandpaper and ethanol. The relative permittivity (ε_r) and dielectric loss (tan δ) were measured at 75–110 GHz microwave frequencies using a Swiss to 12 MCK WR-10 dielectric material characterization text fixture connected to a Keysight P5027A Vector Network Analyzer.

To assess the electrical resistivity, 13 mm diameter and 2 mm thick pellets were prepared and polished. Additionally, 200 nm thick platinum electrodes were Sputter Coated (Quorum Q150R) on both flat surfaces. The samples were subjected to a voltage of 1 V which was held for 4 min to allow for current stabilization using a Hewlett-Packard 4140 B pA Meter/DC Voltage source.

To determine electrical breakdown strength, 13 mm diameter pellets were polished to reduce their thickness from 2 mm to 0.4 mm. The test was conducted applying a DC voltage gradually increasing at a rate of 500 V/s until the electrical breakdown failure occurred on the sample, in reference to the IEEE Std 930™-2004 Guide for the Statistical Analysis of Electrical Insulation Breakdown Data.

For characterization of the anisotropic thermal conductivity of NMO-hBN composite, samples with 40 vol% of filler were fabricated to have 13 mm diameter and 14 mm height. The pellet was cut into two pieces using a slow wire cutter to measure the in-plane direction from one piece and the out-of-plane direction from the other. The thermal conductivity in each anisotropic direction was calculated ($\kappa = \alpha\rho C_p$) using the density (ρ), heat capacity (C_p) and thermal diffusivity (α) determined for each piece of the sample. The thermal diffusivity (α) was measured using a laser flash system (LFA-467 HT HyperFlash®, Germany). Specific heat (C_p) was measured by differential scanning calorimetry (Netzsch DSC 214, Germany). The uncertainties in thermal conductivity was determined to be ±2 %.

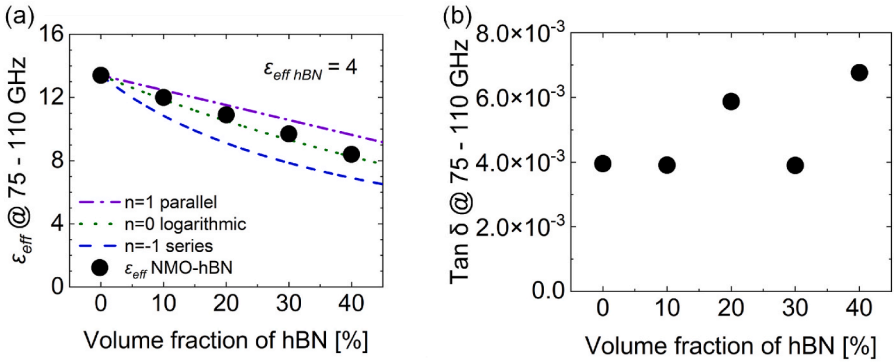

Fig. 1. (a) Evolution of the effective relative permittivity (ε_{eff}) at 75–110 GHz, fitting a logarithmic mixing law with $\varepsilon_{hBN\ eff} = 4$, and (b) corresponding dielectric loss as function of filler volume fraction.

3. Results and discussion

3.1. Dielectric properties at microwave frequencies (75–110 GHz)

Dielectric properties of cold sintered samples were analyzed at 75–110 GHz microwave frequencies. At room temperature, the dielectric constant (ε_r) of composites systematically decreased with increasing filler volume from $\varepsilon_r = 13.4$ in pure NMO, to $\varepsilon r = 8.4$ in NMO-hBN 40 vol % composite. The corresponding dielectric loss ($\tan\delta = \varepsilon''/\varepsilon'$) showed low values between 3.9×10^{-3} and 6.8×10^{-3}. This behavior illustrated in Fig. 1, aligns with previously reported structure-dielectric properties relationship in grain boundary engineered NMO-hBN composites [38] fitting Lichtenecker's mixing power law which considers the spatial connectivity of composite phases [45,46].

$$\widetilde{\varphi}^n = \sum_{i=1}^{N} f_i \varphi_i^n \qquad \text{(Eq. 1)}$$

where φ_i is the property of the ith phase, f_i is the volume fraction of the ith phase. This is summed over the *N*-phases making up the composite. $\widetilde{\varphi}$ is the property that is averaged through the composite mixing, and *n* is the exponent that ranges from $-1 \leq n \leq +1$. The *n* value is indicative of the series or parallel mixing that reflects the spatial connectivity of the respective phases.

Laturia et al. have documented the anisotropic dielectric constant of hBN, noting values of $\varepsilon_{hBN}\| = 6.93$ in plane, and $\varepsilon_{hBN}{}^{\perp} = 3.76$ out of plane [47].

In this study, the effective permittivity of hBN $\varepsilon_{hBN\ eff} = 4$. This value is consistent with previous reports on cold sintered NMO-hBN composites. It primarily reflects the permittivity in the out-of-plane direction ($\varepsilon_{hBN}{}^{\perp}$). This outcome is systematically linked to the engineered microstructure of grain boundaries, where 2D hBN flakes are preferentially aligned perpendicular to the uniaxial pressure applied during cold sintering, a conclusion supported by HR-TEM and STEM imaging [38]. Calculations for the composites' relative permittivity, utilizing a logarithmic mixing law with a limiting exponent n→0 (Eq. (2)), reinforce the suitability of NMO-hBN cold-sintered composites for microwave substrate applications.

$$\log \widetilde{\varepsilon}_r = f_1 \log \varepsilon_{r1} + f_2 \log \varepsilon_{r2} \qquad \text{(Eq. 2)}$$

3.2. Resistivity and fit to percolation theory

The electrical resistivity of NMO-hBN composites varies with filler volume fraction, calculated from the electrical current and pellets' physical dimensions using the following equation:

$$\rho = \frac{R \bullet \pi r^2}{l} \qquad \text{(Eq. 3)}$$

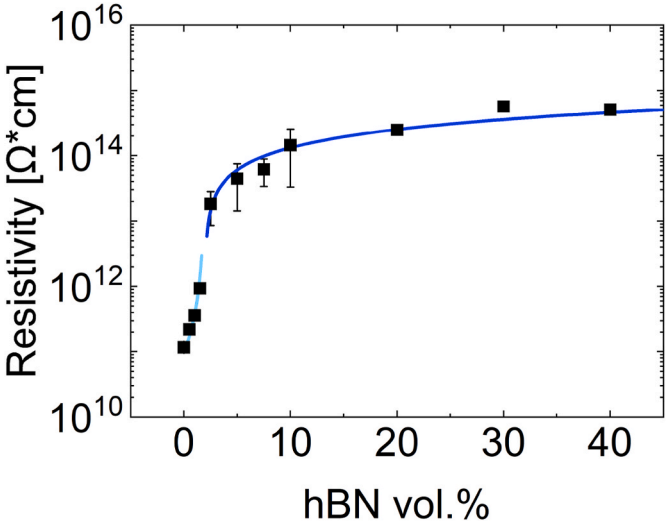

Fig. 2. Resistivity as a function of hBN volume fraction in NMO-hBN composites. Light and dark blue lines on the graph represent fits to equations Eq. (4) and Eq. (5), for regions below and above the 2 vol% percolation threshold, respectively. (For interpretation of the references to colour in this figure legend, the reader is referred to the Web version of this article.)

where ρ, *R*, *r* and *I* respectively represent the resistivity, resistance, radius, and thickness of the pellet.

Pure NMO samples exhibited a resistivity around 10^{11} Ω•cm while composite samples with hBN reached resistivity levels up to 10^{14} Ω•cm. A notable increase in resistivity at 2 vol% hBN, as illustrated in Fig. 2, introduces an intriguing aspect to the concept of percolation, challenging traditional expectations where a filler enhances percolation in a non-conductive matrix. Typically, we consider percolation with a filler phase in a non-conducting matrix. Here we have a reasonable microwave dielectric material, that we add an even higher resistivity material into the grain boundaries. Here the hBN flakes are blocking the conduction paths and thereby improving the resistivity with increasing volume fraction of fillers. This is a most interesting and beneficial observation of the cold sintered composites. It is noteworthy that this change is different from the pure mixing law variation with dielectric and thermal properties.

The 2D nature of the hBN made such behavior possible given its ability to shear upon the applied stress of the press during the cold sintering process. As a result, the sheared layers of resistive hBN easily enveloped the NMO grains, forcing conduction between the NMO grains to first pass through the resistive layer. This dispersion of material amongst the grain boundaries allows for a swifter change in resistive

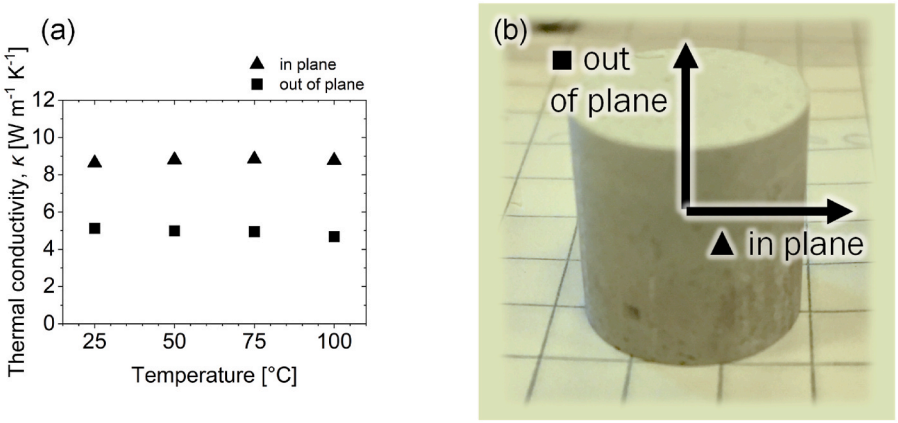

Fig. 3. (a) In-Plane and Out-of-Plane Thermal Conductivity versus Temperature for cold sintered NMO-40 vol% hBN composite. (b) Photo of the NMO-40 vol% hBN composite with measurement directions.

behavior compared to random filler distribution. Shearing the 2D material yields a greater surface area of contact with the NMO grains per volume % of filler as the hBN is wedged between the grain boundaries. The resulting percolation trend for measuring the composite's resistivity is composed of two sections. The fitting curve below the percolation threshold is described by Eq. (4):

$$\rho = \rho_m \left(\frac{\varphi_c - \varphi_f}{\varphi_c} \right)^{-s} \quad \text{(Eq. 4)}$$

where ρ is the effective resistivity of the composite, ρ_m is the resistivity of the ceramic matrix, ϕ_f is the volume fraction of the filler, ϕ_c is the percolation threshold, and s is the critical exponent corresponding to the percolation theory. For the fitting curve above the percolation threshold, the fitting equation (Eq. 5) is

$$\rho = \rho_f \left(\varphi_f - \varphi_c \right)^t \quad \text{(Eq. 5)}$$

where ρ is the effective resistivity of the composite, ρ_f is the resistivity of the filler, ϕ_f is the volume fraction of the filler, ϕ_c is the percolation threshold, and t is the critical exponent corresponding to the percolation theory [48].

For fitting the effective electrical resistivity (ρ) of the composites to percolation theory (Eqs. (4) and (5)), the parameters were as follows: matrix resistivity $\rho_m = 10^{11}$ Ω•cm, filler resistivity $\rho_f = 10^{15}$ Ω•cm, percolation threshold $\phi_c = 2.0$ vol% hBN, and critical exponents s and t at 2.0 and 0.8, respectively. These findings are consistent with numerous studies on 2D materials as fillers, which often report percolation thresholds under 2.0 vol% filler content. This is particularly evident in the electrical properties of composites using materials like graphene as filler [49–52].

3.3. Anisotropic thermal conductivity of NMO-hBN composite

Previous research has shown that thermal conductivity (κ) of cold sintered pure NMO is ~1.7 W m^{-1} K^{-1}, and for NMO-hBN composites it increases with the filler volume, following a logarithmic mixing law with an effective $\kappa_{\text{hBN eff}} = 30$ W m^{-1} K^{-1} [38,53,54]. As previously mentioned, the cold sintering process, involving uniaxial pressure, results in the hBN flakes aligning perpendicularly to the applied force, leveraging its anisotropic thermal conductivity. This anisotropy arises from the strong covalent bonds in the in-plane direction, enhancing thermal management capabilities compared to the out-of-plane direction. For the NMO-40 vol% hBN samples, thermal conductivity was assessed in both directions using Eq. (6):

$$\kappa = \alpha \rho C_p \quad \text{(Eq. 6)}$$

where κ is the thermal conductivity, α is the thermal diffusivity as measured by LFA, ρ is the density and C_p is the specific heat capacity as measured by DSC. Fig. 3 illustrates the anisotropic thermal conductivity of the NMO-40 vol% composite, which remains steady between 25 °C and 100 °C. As anticipated, conductivity is greater in the in-plane direction, a result of the hBN flakes aligning preferentially under the uniaxial pressure applied during the cold sintering process.

3.4. Electrical breakdown strength

From earlier works on cold sintered ceramic matrix composites, it is known that grain boundary inclusions can impact the breakdown field [43,55–57]. It could be anticipated that the controlling breakdown strength in the NMO is a thermal breakdown process. The increase in thermal conductivity and the increase in electrical resistivity should be of benefit to raising dielectric breakdown strength. This is rationalized for the case of thermal breakdown, where there is a balance between the thermal properties and the Joule heating as shown by Eq. (7):

$$C_v \frac{dT}{dt} - div\,(\kappa\, grad\, T) = \sigma E^2 \quad \text{(Eq. 7)}$$

here C_v is the specific heat per unit volume, κ is the thermal conductivity, T is the temperature, t is the time, σ is the electrical conductivity, and E is the applied electric field. Equation (6) is a balance between the heat absorbed and the heat lost to the surroundings with heat conducted away, with the first and second term on the left hand side of the equation, the term on the right hand side is the Joule heating that is continuously being generated from the conduction, and or the dielectric loss mechanism [58,59].

To assess the quality of the solid dielectric strength of the samples, the scatter of the electrical breakdown voltage in the experimental results was analyzed according to the Weibull probability distribution (Eq. (8)):

$$F(V) = 1 - exp\left\{ -\left(\frac{V}{\alpha} \right)^{\beta} \right\} \quad \text{(Eq. 8)}$$

where V is the breakdown voltage, α is the scale parameter which represents the voltage required for 63.2 % of the tested samples to fail, and β is the shape parameter which represents a measure of dispersion of the breakdown voltages [60,61].

Electrical breakdown (E_b) tests on NMO-hBN composites revealed enhanced electrical breakdown strength and β values with hBN addition. While the composite samples show a unimodal distribution according to Weibull statistics, the distribution for pure NMO exhibits a bimodal characteristic, with β values of 5.7 ± 1.2 and 2.7 ± 0.6 as determined

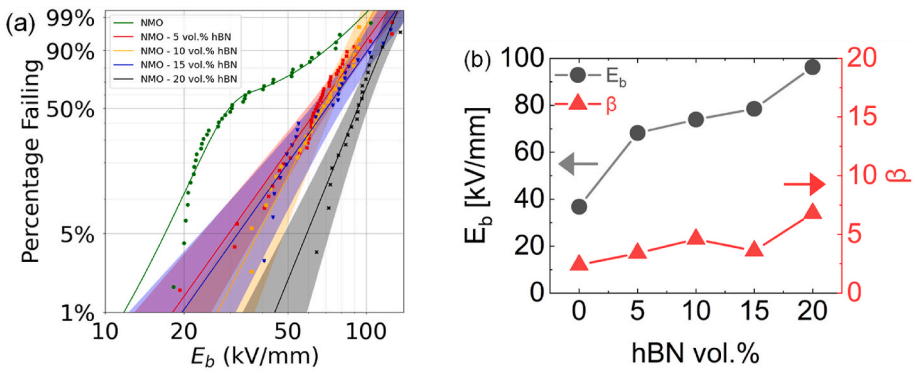

Fig. 4. (a) Weibull statistical analysis and (b) results of Electrical breakdown strength (E_b, β) for NMO-hBN composites as function of filler volume fraction.

through a Weibull mixture model. With the addition of 20 vol% of hBN, the $E_b = 96.3$ kV/mm, approaching the maximum capability limits of the high voltage DC source of 30 kV applied. For samples at 30 vol% and 40 vol% hBN, 30 kV did not induce breakdown, suggesting higher resilience. These samples had a 13 mm diameter and thickness ranging from 0.3 to 0.5 mm. As shown in Fig. 4, Weibull analysis demonstrated consistent improvements in E_b and the shape parameter (β) with increased hBN content, pointing to a narrower breakdown voltage range.

4. Conclusions

Cold sintering was employed to fabricate grain boundary-engineered composites of Sodium Molybdate and hexagonal Boron Nitride, achieving densities over 96 % across filler volume fractions of 0.5–40 vol %. Dielectric testing at 75–110 GHz frequencies and room temperature showed that relative permittivity aligns with the Lichtenecker general mixing law, having an effective hBN permittivity ($\varepsilon_{hBN\ eff}$) of 4 for 10–40 vol% filler fractions, with dielectric loss (tan δ) ranging from 3.9×10^{-3} to 6.8×10^{-3}. The NMO-hBN composites' resistivity increased with filler addition, consistent with percolation theory predictions. A percolation threshold was noted at 2.0 vol% hBN. Then, a significant resistivity increase of three orders of magnitude was observed at 10 vol% hBN, and four orders at 40 vol% hBN. The electrical breakdown strength also improved with increments of hBN in the composite, and not only the insulation breakdown increased, but the shape parameter (β) exhibited higher values compared to the pure NMO material, indicating a reduction in the range of the breakdown voltage with the increase of filler volume fraction. Finally, anisotropic thermal conductivity measurements, influenced by the hexagonal boron nitride's crystal structure, confirmed distinct in-plane and out-of-plane conductivities. These findings on the dielectric, electrical, and thermal behaviors of cold sintered NMO-hBN reinforce its potential as a novel material for high-frequency microwave substrate applications, building upon and extending previously reported properties.

CRediT authorship contribution statement

Javier Mena-Garcia: Writing – original draft, Investigation. **Michael W. Mervosh:** Investigation. **Pedram Yousefian:** Investigation. **Arnaud Ndayishimiye:** Writing – review & editing. **Steven E. Perini:** Investigation. **Wenjie Li:** Investigation. **Bed Poudel:** Investigation. **Clive A. Randall:** Writing – original draft, Supervision, Investigation, Conceptualization.

Declaration of competing interest

The authors declare that they have no known competing financial interests or personal relationships that could have appeared to influence the work reported in this paper.

Acknowledgments

This material is based upon work supported by the National Science Foundation, as part of the Center for Dielectrics and Piezoelectrics under Grant Nos. IIP-1841453 and IIP-1841466. W.L. acknowledges the financial support from the Army RIF program. B.P. acknowledges the financial support from the National Science Foundation through I/UCRC Program. We would like to acknowledge the staff of the Materials Characterization Laboratory at The Pennsylvania State University, for aiding in the work described here and for the use of their equipment. We thank Melissa Bailey for her help to prepare the manuscript. J.M.G. also thanks Dr. Sun Hwi Bang and Dr. Zane Grady for helpful discussions. We also thank the members of the many companies that continue to offer support and ideas to drive this work.

References

[1] M.T. Sebastian, H. Jantunen, Low loss dielectric materials for LTCC applications : a review, Int. Mater. Rev. 53 (2008) 57–90, https://doi.org/10.1179/174328008X277524.
[2] Z. Li, J. Pan, H. Hu, H. Zhu, Recent advances in new materials for 6G, Communications 2100978 (2022) 1–19, https://doi.org/10.1002/aelm.202100978.
[3] S. Funahashi, J. Guo, H. Guo, K. Wang, A.L. Baker, K. Shiratsuyu, C.A. Randall, Demonstration of the cold sintering process study for the densification and grain growth of ZnO ceramics, J. Am. Ceram. Soc. 100 (2017) 546–553, https://doi.org/10.1111/jace.14617.
[4] S.H. Bang, A. Ndayishimiye, C.A. Randall, Mechanistic approach to identify densification kinetics and mechanisms of zinc oxide cold sintering, Acta Mater. (2019), https://doi.org/10.2139/ssrn.3428070.
[5] A. Ndayishimiye, M.Y. Sengul, T. Sada, S. Dursun, S. Hwi, Z.A. Grady, K. Tsuji, S. Funahashi, A.C.T. Van Duin, C.A. Randall, Roadmap for densification in cold sintering : chemical pathways, Open Ceram 2 (2020) 100019, https://doi.org/10.1016/j.oceram.2020.100019.
[6] A. Ndayishimiye, S.H. Bang, C.J. Spiers, C.A. Randall, Reassessing cold sintering in the framework of pressure solution theory, J. Eur. Ceram. Soc. 43 (2023) 1–13, https://doi.org/10.1016/j.jeurceramsoc.2022.09.053.
[7] X. Kang, R. Floyd, S. Lowun, M. Cabral, E. Dickey, J.-P. Maria, Mechanism studies of hydrothermal cold sintering of zinc oxide at near room temperature, J. Am. Ceram. Soc. 102 (2019) 4459–4469, https://doi.org/10.1111/jace.16340.
[8] S. Grasso, M. Biesuz, L. Zoli, G. Taveri, A.I. Duff, D. Ke, A. Jiang, M.J. Reece, A review of cold sintering processes, Adv. Appl. Ceram. 119 (2020) 115–143, https://doi.org/10.1080/17436753.2019.1706825.
[9] B. Nie, T. Liu, M. Alcoutlabi, S. Basu, S. Kumara, M. Li, J. Lian, H. Sun, Cold sintering-enabled interface engineering of composites for solid-state batteries, Front. Energy Res. (2023) 1–7, https://doi.org/10.3389/fenrg.2023.1149103.
[10] J. Guo, S.S. Berbano, H. Guo, A.L. Baker, M.T. Lanagan, C.A. Randall, Cold sintering process of composites: bridging the processing temperature gap of ceramic and polymer materials, Adv. Funct. Mater. 26 (2016) 7115–7121, https://doi.org/10.1002/adfm.201602489.
[11] S. Dursun, K. Tsuji, S.H. Bang, A. Ndayishimiye, C.A. Randall, A route towards fabrication of functional ceramic/polymer nanocomposite devices using the cold sintering process, ACS Appl. Electron. Mater. 2 (2020) 1917–1924, https://doi.org/10.1021/acsaelm.0c00225.
[12] N. Sibi, A. Rajan, G. Subodh, Garnet mineral based composites through cold sintering process: microstructure and dielectric properties, J. Eur. Ceram. Soc. 40 (2020) 371–375, https://doi.org/10.1016/j.jeurceramsoc.2019.09.012.

[13] E. Garcia-Martin, C. Granados-Miralles, S. Ruiz-Gomez, L. Perez, A. del Campo, J. C. Guzman-Minguez, C. de J. Fernandez, A. Quesada, J.F. Fernandez, A. Serrano, Dense strontium hexaferrite-based permanent magnet composites assisted by cold sintering process, J. Alloys Compd. 917 (2022) 165531, https://doi.org/10.1016/j.jeurceramsoc.2019.09.012.

[14] C. Yang, J. Li, X. Wang, D. Yang, H. Shi, S. Meng, S. Du, ZrW_2O_8/ZrO_2 composites with low/near-zero coefficients of thermal expansion fabricated at ultralow temperature: an integration of hydrothermal assembly and a cold sintering process, ACS Appl. Mater. Interfaces 13 (2021) 39738–39747, https://doi.org/10.1021/acsami.1c10108.

[15] M. Liu, Q. Jin, P. Shen, Cold sintering of $NaNO_3$/MgO heat-storage composite, Ceram. Bull. 46 (2020) 28955–28960, https://doi.org/10.1016/j.ceramint.2020.08.066.

[16] Z.M. Grady, Z. Fan, J. Fanghanel, C.A. Randall, Containing a Ceramic Active Material and a Solid- Batteries, 2024, pp. 4492–4512, https://doi.org/10.1039/d3ta07067k.

[17] X. Zhao, J. Guo, K. Wang, T.H. De Beauvoir, B. Li, C.A. Randall, Introducing a ZnO–PTFE (Polymer) nanocomposite varistor via the cold sintering process, Adv. Eng. Mater. 1700902 (2018) 1–8, https://doi.org/10.1002/adem.201700902.

[18] T. Sada, K. Tsuji, A. Ndayishimiye, Z. Fan, Y. Fujioka, C.A. Randall, Enhanced high permittivity $BaTiO_3$–polymer nanocomposites from the cold sintering process, J. Appl. Phys. 128 (2020) 084103, https://doi.org/10.1063/5.0021040.

[19] J. Mena-Garcia, S. Dursun, K. Tsuji, S.H. Bang, Z. Fan, A. Ndayishimiye, C. Randall, Integration and characterization of a ferroelectric polymer PVDF-TrFE into the grain boundary structure of ZnO via cold sintering, J. Eur. Ceram. Soc. 42 (2022) 2789–2797, https://doi.org/10.1016/j.jeurceramsoc.2022.01.064.

[20] Y. Li, M. Zheng, M. Zang, M. Zhu, Y. Hou, Cold sintering co-firing of (Ca, Bi) (Mo, V)O_4–PTFE composites in a single step, J. Am. Ceram. Soc. 105 (2022) 6262–6270, https://doi.org/10.1111/jace.18595.

[21] V.L. Vilesh, N. Santha, G. Subodh, Influence of Li_2MoO_4 and polytetrafluoroethylene addition on the cold sintering process and dielectric properties of $BaBiLiTeO_6$ ceramics, Ceram. Int. 47 (2021) 30756–30763, https://doi.org/10.1016/j.ceramint.2021.07.255.

[22] D.S. Gyan, A. Dwivedi, Structural and electrical characterization of $NaNbO_3$-PVDF nanocomposites fabricated using cold sintering synthesis route, J. Appl. Phys. 125 (2019) 024103, https://doi.org/10.1063/1.5046458.

[23] J. Guo, B. Legum, B. Anasori, K. Wang, P. Lelyukh, Y. Gogotsi, C.A. Randall, Cold sintered ceramic nanocomposites of 2D MXene and zinc oxide, Adv. Mater. 30 (2018) 1–6, https://doi.org/10.1002/adma.201801846.

[24] J. Gao, Q. Ding, P. Yan, Y. Liu, J. Huang, T. Mustafa, R. Guo, X. Lu, K. Wang, S. Sun, X. Feng, W. Luo, Y. Fan, W. Jiang, Highly improved microwave absorbing and mechanical properties in cold sintered ZnO by incorporating graphene oxide, J. Eur. Ceram. Soc. 42 (2022) 993–1000, https://doi.org/10.1016/j.jeurceramsoc.2021.10.053.

[25] J. Guo, M. Si, X. Zhao, L. Wang, K. Wang, J. Hao, H. Wang, C.A. Randall, Altering interfacial properties through the integration of C_{60} into ZnO ceramic via cold sintering process, Carbon N. Y. 190 (2022) 255–261, https://doi.org/10.1016/j.carbon.2022.01.017.

[26] C. Vakifahmetoglu, L. Karacasulu, Cold sintering of ceramics and glasses : a review, Curr. Opin. Solid State Mater. Sci. 24 (2020) 100807, https://doi.org/10.1016/j.cossms.2020.100807.

[27] H. Kähäri, M. Teirikangas, J. Juuti, H. Jantunen, Room-temperature fabrication of microwave dielectric Li_2MoO_4–TiO_2 composite ceramics, Ceram. Int. 42 (2016) 11442–11446, https://doi.org/10.1016/j.ceramint.2016.04.081.

[28] W. Bin Hong, L. Li, H. Yan, X.M. Chen, Cold sintering and microwave dielectric properties of dense HBO_2-II ceramics, J. Am. Ceram. Soc. 102 (2019) 5934–5940, https://doi.org/10.1111/jace.16450.

[29] J. Hao, J. Guo, E. Zhao, M. Si, X. Yuan, F. Yao, H. Wang, Grain size effect on microwave dielectric properties of Na_2WO_4 ceramics prepared by cold sintering process, Ceram. Int. 46 (2020) 27193–27198, https://doi.org/10.1016/j.ceramint.2020.07.200.

[30] H. Kahari, M. Teirikangas, J. Juuti, H. Jantunen, Dielectric properties of lithium molybdate ceramic fabricated at room temperature, J. Am. Ceram. Soc. 97 (2014) 3378–3379, https://doi.org/10.1111/jace.13277.

[31] P. Ramachandran, H. Kahari, J. Juuti, H. Jantunen, Room temperature densified ceramics for weight optimized circular polarized GPS antenna design, Microw. Opt. Technol. Lett. 60 (2018) 1061–1066, https://doi.org/10.1002/mop.31105.

[32] Y. Ji, K. Song, X. Luo, B. Liu, H.B. Bafrooei, D. Wang, Microwave dielectric properties of (1-x) Li_2MoO_4-xMg_2SiO_4 composite ceramics fabricated by cold sintering process, Front. Mater. 6 (2019) 256, https://doi.org/10.3389/fmats.2019.00256.

[33] D. Wang, L. Li, J. Jiang, Z. Lu, G. Wang, K. Song, D. Zhou, I.M. Reaney, Cold sintering of microwave dielectric ceramics and devices, J. Mater. Res. 36 (2021) 333–349, https://doi.org/10.1557/s43578-020-00029-w.

[34] D. Wang, S. Zhang, D. Zhou, K. Song, A. Feteira, Y. Vardaxoglou, W. Whittow, D. Cadman, I.M. Reaney, Temperature stable cold sintered $(Bi_{0.95}Li_{0.05})(V_{0.9}Mo_{0.1})O_4$-$Na_2Mo_2O_7$ microwave dielectric composites, Materials 12 (2019) 1–10, https://doi.org/10.3390/ma12091370.

[35] D. Wang, J. Chen, G. Wang, Z. Lu, S. Sun, J. Li, J. Jiang, D. Zhou, K. Song, I. M. Reaney, Cold sintered LiMgPO4 based composites for low temperature co-fired ceramic (LTCC) applications, J. Am. Ceram. Soc. 103 (2020) 6237–6244, https://doi.org/10.1111/jace.17320.

[36] J. Guo, A.L. Baker, H. Guo, M. Lanagan, C.A. Randall, Cold sintering process : a new era for ceramic packaging and microwave device development, J. Am. Ceram. Soc. 100 (2017) 669–677, https://doi.org/10.1111/jace.14603.

[37] I.J. Induja, M.T. Sebastian, Microwave dielectric properties of mineral sillimanite obtained by conventional and cold sintering process, J. Eur. Ceram. Soc. 37 (2017) 2143–2147, https://doi.org/10.1016/j.jeurceramsoc.2017.01.007.

[38] J. Mena-Garcia, A. Ndayishimiye, Z. Fan, S.E. Perini, B. Foley, J. Gaskins, C. A. Randall, Sodium molybdate-hexagonal boron nitride composites enabled by cold sintering for microwave dielectric substrates, J. Am. Ceram. Soc. (2023) 1–11, https://doi.org/10.1111/jace.19254.

[39] D.G. Cahill, W.K. Ford, K.E. Goodson, G.D. Mahan, A. Majumdar, H.J. Maris, R. Merlin, S.R. Phillpot, Nanoscale thermal transport, J. Appl. Phys. 93 (2017) 793–818, https://doi.org/10.1063/1.1524305.

[40] D.G. Cahill, P. V Braun, G. Chen, D.R. Clarke, S. Fan, K.E. Goodson, P. Keblinski, W. P. King, G.D. Mahan, A. Majumdar, H.J. Maris, S.R. Phillpot, E. Pop, L. Shi, Nanoscale thermal transport. II. 2003–2012, Appl. Phys. Rev. 011305–1 (2014), https://doi.org/10.1063/1.4832615.

[41] C. Yu, J. Zhang, W. Tian, X. Fan, Y. Yao, Polymer composites based on hexagonal boron nitride and their application in thermally conductive composites, RSC Adv. 8 (2018) 21948–21967, https://doi.org/10.1039/c8ra02685h.

[42] A. Vetser, Cold Sintering of $Na_2Mo_2O_7$ Hexagonal BN Composites for MLCC Applications, The Pennsylvania State University, 2023.

[43] J. Guo, N. Pfeiffenberger, A. Beese, A. Rhoades, L. Gao, A. Baker, K. Wang, A. Bolvari, C.A. Randall, Cold sintering $Na_2Mo_2O_7$ ceramic with Poly(ether imide) (PEI) polymer to realize high-performance composites and integrated multilayer circuits, ACS Appl. Nano Mater. 1 (2018) 3837–3844, https://doi.org/10.1021/acsanm.8b00609.

[44] A. Ndayishimiye, Z. Fan, J. Mena-Garcia, J.M. Anderson, C.A. Randall, Coalescence in cold sintering: a study on sodium molybdate, Open Ceram 11 (2022) 100293, https://doi.org/10.1016/j.oceram.2022.100293.

[45] A.V. Goncharenko, V.Z. Lozovski, E.F. Venger, Lichtenecker's equation: applicability and limitations, Opt Commun. 174 (2000) 19–32, https://doi.org/10.1016/S0030-4018(99)00695-1.

[46] K. Kata, Y. Shimada, H. Takamizawa, Low dielectric constant new materials for multilayer ceramic substrate, IEEE trans. Components, hybrids manuf, Technol. 13 (1990) 448–451, https://doi.org/10.1016/S0030-4018(99)00695-1.

[47] A. Laturia, M.L. Van de Put, W.G. Vandenberghe, Dielectric properties of hexagonal boron nitride and transition metal dichalcogenides: from monolayer to bulk, Npj 2D Mater. Appl. 6 (2018), https://doi.org/10.1038/s41699-018-0050-x.

[48] O. Maruzhenko, Y. Mamunya, G. Boiteux, S. Pusz, U. Szeluga, S. Pruvost, Improving the thermal and electrical properties of polymer composites by ordered distribution of carbon micro- and nanofillers to cite this version : HAL Id : hal-02136462, Int. J. Heat Mass Tran. 138 (2019) 75–84.

[49] H. Zhang, W. Zheng, Q. Yan, Y. Yang, J. Wang, Z. Lu, G. Ji, Z. Yu, Electrically conductive polyethylene terephthalate/graphene nanocomposites prepared by melt compounding, Polymer 51 (2010) 1191–1196, https://doi.org/10.1016/j.polymer.2010.01.027.

[50] X.-Y. Qi, D. Yan, Z. Jiang, Y.-K. Cao, Z.-Z. Yu, F. Yavari, N. Koratkar, Enhanced electrical conductivity in polystyrene nanocomposites at ultra-low graphene conteng, ACS Appl. Mater. Interfaces 3 (2011) 3130–3133, https://doi.org/10.1021/am200628c.

[51] S. Wu, R.B. Ladani, J. Zhang, E. Bafekrpour, K. Ghorbani, A.P. Mouritz, A. J. Kinloch, C.H. Wang, Aligning multilayer graphene flakes with an external electric field to improve multifunctional properties of epoxy nanocomposites, Carbon N. Y. 94 (2015) 607–618, https://doi.org/10.1016/j.carbon.2015.07.026.

[52] A.J. Marsden, D.G. Papageorgiou, C. Valles, A. Liscio, V. Palermo, M.A. Bissett, R. J. Young, I.A. Kinloch, Electrical percolation in graphene – polymer composites, 2D Mater. 5 (2018), https://doi.org/10.1088/2053-1583/aac055.

[53] Y. Hirata, T. Shimonosono, Mixing rules of Young's modulus, thermal expansion coefficient and thermal conductivity of solid material with particulate inclusion, J. Korean Ceram. Soc. 53 (2016) 43–49, https://doi.org/10.4191/kcers.2016.53.1.43.

[54] W. Li, J. Wang, B. Poudel, H.B. Kang, S. Huxtable, A. Nozariasbmarz, U. Saparamadu, S. Priya, Filiform metal silver nanoinclusions to enhance thermoelectric performance of P type $Ca_3Co_4O_{9+\delta}$, ACS Appl. Mater. Interfaces 11 (2019) 42131–42138, https://doi.org/10.1021/acsami.9b13607.

[55] J. Guo, X. Zhao, T.H. De Beauvoir, J. Seo, S.S. Berbano, A.L. Baker, C. Azina, C. A. Randall, Recent progress in applications of the cold sintering process for ceramic, Polym. Compos. 1801724 (2018) 1–15, https://doi.org/10.1002/adfm.201801724.

[56] M. Si, J. Guo, J. Hao, X. Zhao, C.A. Randall, H. Wang, Cold sintered composites consisting of PEEK and metal oxides with improved electrical properties via the hybrid interfaces, Composer Part B. 226 (2021) 109349, https://doi.org/10.1016/j.compositesb.2021.109349.

[57] T. Sada, K. Tsuji, A. Ndayishimiye, Z. Fan, Y. Fujioka, C.A. Randall, Highly reliable $BaTiO_3$ -polyphenylene oxide nanocomposite dielectrics via cold, Sintering 2100963 (2021) 1–11, https://doi.org/10.1002/admi.202100963.

[58] J.J. O'Dwyer, Theory of dielectric breakdown in solids, Electrochem. Soc. 116 (1969).

[59] L.A. Dissado, C. Fothergill, Electrical Degradation and Breakdown in Polymers, The Institution of Engineering and Technology, London, United Kingdom, 1992.

[60] E.A. Feilat, S. Grzybowski, P. Knight, L. Doriott, Breakdown and aging behavior of composite insulation system under DC and AC high voltages 2 assessment of HV insulation system, WSEAS trans. Circuits syst. https://www.researchgate.net/publication/258342893_Breakdown_and_aging_behavior_of_composite_insulation_system_under_DC_and_AC_high_voltages, 2016.

[61] C. Chauvet, C. Laurent, Weibull statistics in short-term dielectric breakdown of thin polyethylene films, IEEE Trans. Electr. Insul. 28 (1993) 18–29.